Supplementary Materials for

Spatial Organization of Cytokinesis Signaling Reconstituted in a Cell-Free System

Phuong A. Nguyen[1,2]*, Aaron C. Groen[1,2]*, Martin Loose[1], Keisuke Ishihara[1,2], Martin Wühr[1], Christine M. Field[1,2]†‡, Timothy J. Mitchison[1,2]†

[1]Department of Systems Biology, Harvard Medical School, Boston, MA 02115, USA.
[2]Marine Biological Laboratory, Woods Hole, MA 02543, USA.

* These authors contributed equally to this work.

† These authors contributed equally to this work.

‡ Corresponding author. E-mail: Christine_Field@hms.harvard.edu

This PDF file includes:

Materials and Methods
Supplementary Text
Figs. S1 to S13
Tables S1 to S2
Captions for Movies S1 to S10

Other Supplementary Materials for this manuscript includes the following:

Movies S1 to S10

Materials and Methods

Antibodies

Antibodies were raised in rabbits to GFP-fused *X. laevis* Aurora kinase A (full-length), Kif20A (C-terminal 359 amino acids), and Kif23 (C-terminal 309 amino acids), as well as GST-fused Kif20AE (C-terminal 190 amino acids). Antisera were first depleted of GFP or GST antibodies, then antibodies were affinity purified using the respective fusion protein. For antibodies against Aurora kinase A, antisera were depleted against Aurora kinase B to ensure that the purified antibody was specific to Aurora kinase A and did not perturb kinase activity. DNA for fusion constructs was purchased (GenScript, NJ) and subcloned with Gibson cloning.

Affinity purified C-terminal peptide (CTP) antibodies (rabbit) were produced against *X. laevis* Kif23 (C-EMRAGSNLGPGYEHHVVSKRRRP) and Kif20AE (C-KRTTSKSQEKPEEVSGTSRKRPLLSRR) (NeoBioLab, MA).

Antibodies (rabbit) generated to MBP-fused C-terminal 316 amino acids of *X. laevis* Kif4A (or Xklp1; construct kindly provided by Isabelle Vernos [ICREA, Spain]) were affinity purified (depleted of MBP antibodies). Antibodies (rabbit) generated to GST fused to the N-terminal 100 amino acids of *X. laevis* Aurora kinase B were kindly provided by Ryoma Ohi (Vanderbilt University, TN). See table S1 for sequence information on the proteins studied in this paper.

Antibodies against anillin (*20*) and septin 7 (*22*) were from previous studies. Tubulin antibodies (Sigma #T6074) were purchased.

Antibodies were labeled on column with Alexa-488, Alexa-568, or Alexa-647 dyes (Life Technologies, NY) as previously described (*23*).

Protein Expression Plasmid Constructs

The following constructs were received as kind gifts: Lifeact-GFP construct (*18*) from David Burgess (Boston College, MA), human EB1-GFP construct from Kevin Slep (UNC Chapel Hill, NC), *X. laevis* Kif4A-GFP construct (aka Xklp1-GFP) in pFastBac1 baculovirus expression vector (*13*) from Thomas Surrey (London Research Institute, UK).

The Rho GTPase-binding domain (rGBD) of mouse Rhotekin (amino acids 7-82) was subcloned into pGEX-4T-1 bacterial expression vector with an N-terminal 6xHis-mCherry tag, replacing the GST tag between EcoN1/Not1 restriction sites, creating mCherry-rGBD. The Rhotekin fragment (rGBD) specifically binds to active, GTP-bound RhoA (*16*). Mouse Rhotekin gene was a gift from William Bement (University of Wisconsin–Madison, WI).

The *X. laevis* DasraA gene (IRBHp990G0393D, Source Bioscience, UK) was subcloned into pGEX-4T-1 with an N-terminal 6xHis-eGFP tag, creating GFP-DasraA.

The *X. laevis* PRC1embryonic (PRC1E) gene (codon optimized for *E. coli* and insect cell expression; GenScript, NJ) was subcloned into pET-28b bacterial expression vector with an N-terminal Strep-tag (WSHPQFEK) followed by an eGFP tag, creating GFP-PRC1E. This is an embryonic paralog of the PRC1 gene in *Xenopus* that we called ‘PRC1L’ in a previous publication (*14*).

All subcloning was performed with Gibson cloning. See table S1 for sequence information on the *Xenopus* proteins studied in this paper.

Protein Expression and Purification

EB1-GFP-His, His-mCherry-rGBD (Rho GTPase binding domain), His-GFP-DasraA were conventionally purified from *E. coli* (Rosetta2(DE3)pLysS). Purification of EB1-GFP-His was previously described (*7*). Briefly, expressing cells were lysed by sonication in ice-cold lysis buffer A (50mM NaPi, pH 7.7, 500mM NaCl, 0.1mM $MgCl_2$, 1% Triton X-100, 1mM dithiothreitol [DTT], 1mM phenylmethylsulfonyl fluoride [PMSF]). Clarified lysates were batch-incubated for 1.5 hr at 4°C with HisPur Cobalt resin (~2 mL/L of culture; Thermo Scientific, MA). After elution in lysis buffer containing 300mM imidazole, proteins were gel filtered using a Superdex 75 10/300 GL column (GE Healthcare, MA) equilibrated with 10mM K-HEPES, pH 7.7, 150mM KCl, 1mM DTT. Proteins were supplemented with 10% (w/v) sucrose and flash-frozen in liquid nitrogen for storage at −80°C. Coomassie-stained gels are shown for mCherry-rGBD and GFP-DasraA in fig. S13.

Strep-GFP-PRC1E was expressed in *E. coli* (Rosetta2(DE3)pLysS) after induction with 0.5mM IPTG for 3-4 hrs at 18°C. Expressing cells were lysed by sonication in ice-cold lysis buffer B (50mM NaPi, pH 7.7, 400mM NaCl, 3mM EDTA, 10mM β-mercaptoethanol, Halt Protease Inhibitor Cocktail [Thermo Scientific, MA], 1mg/mL lysozyme, 10μg/mL DNase). Clarified lysates were loaded onto a Strep-Tactin column (IBA GmbH, Germany). After protein binding, column was washed with buffer C (50mM NaPi, 400mM NaCl, 3mM EDTA, 50mM arginine, 50mM glutamate, pH 7.7), then with buffer D (10mM K-Hepes, pH 7.7, 500mM KCl). Protein was eluted with buffer D containing 2.5mM desthiobiotin (Sigma #D1411), supplemented with 1mM DTT and 20% (w/v) sucrose, and flash-frozen in liquid nitrogen for storage at −80°C. Coomassie-stained gels are shown for GFP-PRC1E in fig. S13.

Kif4A-GFP-His was purified from Sf21 insect cells as previously described (*13*) with the following modification: after elution from the HisPur Cobalt column, the protein was gel filtered using a Superose 6 10/300 GL column (GE Healthcare, MA) equilibrated with 10mM K-Hepes, pH 7.7, 500mM KCl, 1mM $MgCl_2$, 0.2mM ATP, 1mM DTT. Protein was supplemented with 20% (w/v) sucrose, and flash-frozen in liquid nitrogen for storage at −80°C.

Tubulin was purified from bovine brain and labeled with X-rhodamine, Alexa488, Alexa568, or Alexa647 dyes (Life Technologies, NY) as previously described (*23*). Purified Lifeact-GFP was a kind gift from David Burgess (Boston College, MA).

Protein concentrations were determined by Bradford assay with BSA standards, and refer to dimers for tubulin and monomers for all the other proteins. See table S1 for sequence information on the *Xenopus* proteins studied in this paper.

Preparation of *Xenopus* Egg Cytoplasm with Intact Actin

Metaphase arrested *Xenopus* egg extracts with intact actin were prepared as described (*3*). Briefly, eggs were dejellyed and processed at 16°C, and immediately crushed at ~12,500xg for 15 min at 4°C. The cytoplasmic layer was isolated, supplemented with protease inhibitors

(leupeptin, pepstatin chymostatin; Sigma) and 50mM sucrose, and immediately stored at 4°C. Egg quality varied from frog to frog, thus batches of eggs from different female frogs were processed separately and the corresponding extracts were never pooled. Extracts from each batch were assayed for actin contractility (*3*) and AAIZ formation between glass coverslips (see below). Only extracts that exhibited strong actin contractility, assembled dense microtubule asters, and formed robust AAIZs, were selected for further experiments.

Aster Assembly Assay Between Glass Coverslips (see fig. S1A and Fig. 1A)

For each experiment, ~50μL of extract was supplemented with fluorescent probes (directly labeled tubulin, directly labeled antibodies, GFP-tagged proteins). Extract was treated with 0.4mM $CaCl_2$ and incubated at 20°C for 2 min to mimic fertilization and induce metaphase-to-interphase transition (referred to as activated extract). Activated extract was incubated on ice for 2 min to depolymerize microtubule and F-actin polymers. Then extract was supplemented with Aurora A antibody-coupled Protein A Dynabeads (Life Technologies, NY) which served as artificial centrosomes (*4*), and placed between two PEG-passivated glass coverslips (~10-15μm deep, or ~5μL extract for a 18mm X 18mm glass coverslip prep; see workflow in fig. S1A). Coverslips were passivated with silane-PEG as described (*3*). Aster assembly reactions were monitored with a widefield or spinning disc confocal microscope at 20°C.

A description of the cell cycle state of our extract system can be found in our recent methods paper (*3*). Judging by immunoblots of proteins that report on Cdk1 phosphorylation status, some mitotic Cdk1 sites were lost as soon as 5 min after calcium addition, while others took up to 20 min to be lost. These findings are consistent with previous observations that different Cdk1 substrates are dephosphorylated at different rates following the fertilization-induced calcium pulse, which breaks the metaphase (CSF) arrest state. We conclude that calcium addition caused the extract to begin to enter the interphase state within a few minutes, but that the full interphase state was not reached until approximately 20 min after calcium addition. AAIZs started forming after about 15 min, and remained for at least 20 min, so their assembly occurred in the full interphase state.

For TIRF imaging, extract was placed between a PEG-passivated and a kappa-casein coated coverslip. Kappa-casein (Sigma #C0406) coating minimized the adsorption of many microtubule-interacting proteins on the glass, while it still allowed microtubules to track along the coated surface (*3*).

For visualization, fluorescent probes were used at the following concentrations: 250nM Alexa488-, 568- or 647-tubulin, 40nM EB1-GFP, 10nM Kif4A-GFP, 20nM GFP-PRC1E, 20nM GFP-DasraA, and 0.1-1 μg/mL Alexa674-IgG against AurkB to visualize the CPC, Alexa568-IgG against a Kif23-CTP to visualize the Centralspindlin complex, Alexa568-IgG against a Ki20AE-CTP to visualize Kif20AE.

Aster Assembly Assay on Lipid Bilayer Coated Coverslips (see Fig. 3A)

Supported lipid bilayers (SLBs) were prepared in a reaction chamber consisting of a plastic ring glued on plasma-cleaned glass coverslips as previously described (*15*) with modifications in lipid compositions (*24*). Small unilamellar vesicles (SUVs) were prepared by

sonication from porcine brain PC, porcine brain PS, and porcine liver PI (Avanti Polar Lipids, AL) at the molar ratio of 0.6/0.3/0.1 and 5mM total lipid concentration in high salt extract buffer XB (10mM K-Hepes, pH 7.7, 300mM KCl, 1mM $MgCl_2$, 0.1mM $CaCl_2$, 50mM sucrose). The SUV suspension was diluted to 1mM, added to the reaction chamber, and vesicle fusion was induced by adding 0.1mM $CaCl_2$. After 30-60 min incubation at 42°C, lipid bilayers were extensively washed with extract buffer XB (10mM K-Hepes, pH 7.7, 100mM KCl, 1mM $MgCl_2$, 0.1mM $CaCl_2$, 50mM sucrose), and stored at 4°C till experiment.

Note that *Xenopus* egg extracts made on different days varied in their ability to promote actin polymerization at the cortical layer, and we found that adding porcine brain $PI(4,5)P_2$ (Avanti Polar Lipids, AL) up to 1% of the total lipid mixture was sometimes necessary to observe actin enrichment at the AAIZs. We routinely prepared SLBs containing 0%, 0.1%, and 0.5% $PI(4,5)P_2$ for each extract and assayed for cortical actin morphology (alignment along microtubule asters and enrichment at AAIZs) at the beginning of each experiment to determine which $PI(4,5)P_2$ concentration to use for that particular extract.

For each experiment, 60μL of extract was treated with 0.4mM $CaCl_2$ and incubated at 20°C for 10 min, then returned to ice for 2 min. Bilayers were washed 2 times with 20μL extract each, and finally 20μL extract containing fluorescent probes and AurkA beads was layered on top of the bilayer. Aster assembly reactions were monitored with an inverted TIRF or spinning disc confocal microscope at 20°C.

For visualization, fluorescent probes were used at the following concentrations: 250nM Alexa488- or 568-tubulin, 140nM mCherry-rGBD to visualize RhoA-GTP, 140nM Lifeact-GFP to visualize F-actin, and 0.1-1μg/mL Alexa674-IgG against AurkB to visualize the CPC, Alexa568-IgG against a Kif23-CTP to visualize Centralspindlin, Alexa568-IgG against Anillin to visualize Anillin, and Alexa647-IgG against septin 7 to visualize the septin complex.

Immunodepletions, Protein Addback, and Drug Inhibitions
(related to Fig. 1, E and F, Figs. 2 and 3, Fig. 4D, figs. S5, S6, S10)

Kif4A, Kif23, Kif20A, and Kif20AE were depleted using 2 rounds of 20μg of IgG (raised against their C-terminal tail) conjugated to 50μL Protein A Dynabeads (Life Technologies, NY) for 50μL of extracts. Depletions using beads coated with random rabbit IgG served as controls. Depletions were confirmed by Western blots (fig. S6) and loss of localization of labeled antibodies against the depleted proteins in the aster assembly assay. Kif4A depletion phenotype was rescued by adding back 100nM Kif4A-GFP.

For drug inhibition experiments, 100μM ZM447439 (Aurora B kinase inhibitor; Tocris Bioscience, MN), 100μM STLC (S-trityl-l-cysteine; Eg5 inhibitor; Sigma), 100μM GSK-923295 (CenpE inhibitor; MedChem Express, NJ), or 100μM nocodazole (microtubule depolymerizer; Sigma) was added to calcium activated extracts, and samples were prepared and imaged as described above.

All immunodepletion and drug inhibition experiments were performed with $N \geq 3$ biological repeats, using extracts prepared from eggs produced by different female frogs.

Light Microscopy

Widefield images were obtained using a 20X Plan Apo 1.4 NA objective lens (Nikon) on an upright Nikon Eclipse 90i microscope equipped with a Prior Lumen 200 metal arc lamp, a Prior ProScan III motorized XY stage, a Hamamatsu ORCA-ER cooled CCD camera, and driven by Metamorph image acquisition software (Molecular Devices, CA).

Spinning disc confocal images were obtained using a 40X oil Plan Apo 1.30 NA objective lens (Nikon) on an upright Nikon Eclipse E800 microscope equipped with a Melles Griot Krypton/Argon ion laser (488nm, 568nm, 647nm), a Yokogawa CSU-10 spinning disc (Perkin Elmer, MA), a Hamamatsu ORCA-ER cooled CCD camera, and driven by Metamorph.

Confocal Z-stack images were obtained at the Nikon Imaging Center at Harvard Medical School using a 60X oil Plan Apo 1.49 NA objective lens (Nikon) on a confocal Nikon Ti motorized inverted microscope equipped with a Yokogawa CSU-X1 spinning disc (Spectral Applied Research Aurora Borealis modification), Perfect focus, a Prior Proscan II motorized stage, a Spectral Applied Research LMM-5 laser merge module (Ex:Em 488:480/40, 561:620/60, 642:700/75) with AOTF controlled solid state lasers, a Hamamatsu ORCA-AG cooled CCD camera, and driven by Metamorph.

Fixed *Xenopus* embryos were imaged with a laser scanning confocal microscope at the Nikon Imaging Center at Harvard Medical School. A 10X dry and a 20X multi-immersion objective (Nikon) was used on a Nikon Ti-E inverted microscope with a Nikon A1R point scanning confocal head, driven by NIS-Elements image acquisition software.

Some TIRF images were obtained at the Nikon Imaging Center at Harvard Medical School using a 60X Apo TIRF 1.49 NA objective lens (Nikon) on a Nikon Ti-E motorized inverted microscope equipped with a Nikon motorized TIRF illuminator, Perfect focus, a Prior Proscan II motorized stage, Agilent MLC400B laser launch (488nm, 561nm, 647nm), an Andor DU-897 EM-CCD camera driven by NIS-Elements image acquisition software.

Some TIRF images were obtained at Woods Hole with a Nikon Ti-E motorized inverted microscope with a Nikon motorized TIRF illuminator and Agilent MLC400B laser launch (488nm, 561nm, 647nm) with Perfect focus.

Microtubule Plus Tip Tracking: Image Acquisition, Processing and Analysis
(see fig. S2 and Fig. 1E)

Extract was supplemented with 250nM Alexa568-tubulin, 40nM EB1-GFP, and 1μg/mL Alexa647-IgG against AurkB to visualize the CPC. Asters were assembled between PEG-passivated glass coverslips as described above, simultaneously for samples treated with 100μM ZM447439 (AurkB specific inhibitor) and control buffer. Multiple AAIZs were imaged between 20 and 50 minutes of the assembly reaction at 20°C, alternating between control and treatment conditions. A spinning disc confocal microscope with a 40x oil objective (NA = 1.30) was used to acquire images with 2x2 binning. Time-lapse image sequences were acquired of EB1-GFP with 1.5 sec intervals for a total duration of 2 min. Images of tubulin and AurkB were acquired at the beginning and end of each sequence.

To correct for the flow of cytoplasm between the passivated coverslips, EB1 image sequences were registered using the *StackReg* ImageJ plugin with rigid body transformation. The *plusTipTracker* Matlab software was used to perform automated detection and frame-to-frame linking of EB1 to obtain growth tracks (see table S2 for parameters) (*25*). Here we were only interested in the direction of microtubule plus tip growth, not its dynamics, thus we disabled the software's ability to infer plus tip shrinkage events by restricting the 'maximum gap length' to 2 frames. This setting still allowed for inferred forward gaps due to potential error in comet detection, but minimized the number of inferred backward gaps. The frame-to-frame XY coordinates of each tracked comet were extracted from the software's output for further analysis in Matlab.

Tracks were filtered out and excluded from analysis based on the following criteria:

a) Mean intensity of detected particles within a single track is above 99th percentile of the intensity distribution of all detected particles. This is to filter out tracks associated with centrosome beads, bright aggregates and hot pixels that are not stationary because of image registration.

b) Tracks with lifetime longer than 1 min. This is to filter out tracks associated with less bright hot pixels.

c) Tracks with lifetime longer than 20 sec and with mean speed lower than 10μm/min. This is to filter out tracks associated with less bright hot pixels.

Tracks were plotted and colored according to their mean direction.

Aster-Aster Interpenetration Analysis (see fig. S3 and Fig. 1F)

All EB1 comets detected over the time-lapse sequence of 2 min were divided into two populations based on their direction with respect to the axis defined by the interaction zone: 0-180° (blue) and 180-360° (red). This was an approximation for which aster the microtubule originated from. Rectangular regions of interest (ROIs) with a length of 90μm and width of 10μm that were perpendicular to and bisected by the interaction zone were drawn across the image space. Each ROI was divided into 9 square bins with 10μm edges. For each ROI, the fraction of blue/red comets were calculated for each bin and plotted against distance along the length of the ROI (roughly corresponding to the bead-to-bead axis). The plots were visually inspected and outlying data were removed. Data from 50+ ROIs from 5+ interaction zones were pooled and the mean values of all fractions and their standard deviations were determined for each bin, and plotted as a function of distance. The complementary red/blue fractions were also calculated and plotted against distance (fig. S3). Mean blue/red fractions are plotted as a blue solid line, and the complementary mean red/blue fractions as a red solid line in Fig. 1F, where shaded areas represent standard deviations.

Velocity Measurements for CPC Movement (see figs. S7, S10, and Fig. 2, E and F)

Extract was supplemented with 250nM Alexa568-tubulin and 1μg/mL Alexa647-IgG against AurkB to visualize the CPC. Asters were assembled between PEG-passivated glass

coverslips as described above and AAIZs were imaged between 20 and 50 minutes of the assembly reaction at 20°C. A spinning disc confocal microscope with a 40x oil objective (NA = 1.30) was used to acquire images with 2x2 binning. Time-lapse image sequences were acquired of the CPC at the AAIZ with 1.43 sec intervals for a total duration of 1.5-3 min. The most representative image sequences were selected for analysis.

To correct for the flow of cytoplasm between the passivated coverslips, CPC image sequences were registered using the *StackReg* ImageJ plugin with rigid body transformation. A segmented line (3 pixels wide) was manually drawn over the CPC-positive microtubule bundles in each image frame in ImageJ (fig. S7A), and kymographs were generated to show the frame-to-frame fluorescence intensities along these lines (fig. S7B).

For each kymograph, individual tracks of CPC clusters were marked with a segmented line in ImageJ, and coordinates of the tracks were imported into Matlab for further analysis (fig. S7C, Step 1). The position of the CPC cluster was interpolated for each time point ($d_i(t_i)$), and the instantaneous velocity of the CPC cluster was estimated as:

$$v_i(t_i) = \frac{\Delta d_i}{\Delta t_i} = \frac{d_i - d_{i-1}}{t_i - t_{i-1}}$$ (fig. S7C, Step 2).

The distance between the CPC cluster and the CPC-bright midpoint was determined for each time point ($D_i(t_i)$) (fig. S7C, Step 3), and v_i was plotted against D_i for each track (fig. S7C, Step 4). Data from 3+ kymographs were pooled and binned along the D_i axis by 1μm intervals, and the mean CPC velocity with standard deviation was calculated for each interval (fig. S7C, Step 5). Mean CPC velocities are plotted against distance as solid lines in Fig. 2F, where error bars represent standard deviations.

The same analysis was performed for AAIZs assembled with extracts where Kif4A was depleted (fig. S10, A to C) and where Kif4A depletion was followed by addback of 100nM recombinant Kif4A-GFP (fig. S10, D to F).

Velocity Measurements for CPC-Independent Kif4A Movement (see fig. S9)

Extract was supplemented with 250nM Alexa647-tubulin and 3nM Kif4A-GFP. Asters were assembled between a PEG-passivated glass coverslip and a partially passivated coverslip coated with kappa-casein (*3*, *23*), which allows microtubules to track along the kappa-casein-coated side of the coverslip sandwich. A growing aster edge was imaged at 20 min of aster assembly reaction at 20°C. A TIRF microscope with a 60x TIRF objective (NA = 1.49) was used to acquire a two-color time-lapse sequence with 2.1 sec intervals (fig. S9A).

We observed that at the edges of expanding asters, Kif4A loaded onto antiparallel microtubule overlaps that transiently formed between radially outwards growing microtubules and isolated microtubules that grew in the opposite direction (Fig. S9A). These antiparallel overlaps recruited PRC1E, the binding partner of Kif4A that preferentially crosslinks antiparallel microtubules, but not the CPC. Kymographs along microtubules that formed these overlaps allowed us to visualize Kif4A movement in the absence of recruited CPC (Fig. S9B). After correcting for microtubule sliding from tubulin images, we obtained a mean velocity of 26.4±4.1

μm/min (mean±SD) from N=34 tracked Kif4A particles (Fig. S9C). This was the maximal Kif4A velocity we observed in our extract system on interphase asters, as within AAIZs Kif4A slowed down. The reason we observe Kif4A movement in situ at ~half the velocity of that seen with pure protein is unclear (*13*). One possibility is that other microtubule-associated proteins (MAPs) bound to microtubules slowed movement.

Co-localization of Moving Kif4A and Moving CPC (see fig. S11)

Extract was supplemented with 250nM Alexa568-tubulin, 0.1μg/mL Alexa674-IgG against AurkB, and 3nM Kif4A-GFP. Asters were assembled between a PEG-passivated glass coverslip and a partially passivated coverslip coated with kappa-casein. AAIZs were imaged at 50 min of aster assembly reaction at 20°C. A TIRF microscope with a 60x TIRF objective (NA = 1.49) with an additional magnification using a 1.5 optovar was used to acquire a two-color time-lapse sequence with 2.73 sec intervals. Kymographs along antiparallel microtubules bundles were created as described above (fig. S11).

Tubulin Speckle Imaging (see fig. S8)

Asters were assembled between two PEG-passivated glass coverslips, and AAIZs were imaged with either a 100X oil objective with 2x2 binning on a widefield microscope (fig. S8A) or a 60X oil objective with 2x2 binning on a spinning disc confocal microscope (fig. S8B). Extract was supplemented with 250nM X-rhodamine-tubulin and 40nM EB1-GFP for the widefield sample, and 1nM Alexa647-tubulin for the confocal sample. Kymographs along the microtubule bundles were created as described above.

TIRF Image Background Correction and Stitching
(related to Fig. 3, B and C, Fig. 4A, and fig. S12)

The *Scan Large Image* function of the NIS Elements image acquisition software was used to acquire 5x5 to 7x7 adjacent areas with 15% overlap. We refer to the small image captured of one area as a 'tile.' To correct for the dark grid in the large stitched image due to uneven illumination across the image area, a median image was obtained from all individual tiles and normalized to the range 0-1 to obtain a correction image. All individual tiles were then divided by the correction image. The background corrected tiles were stitched into a large image using the *Grid/Collection stitching* ImageJ plugin. Regions of interest were cropped for display. All image processing was done in ImageJ.

3D Reconstructions of Z Stacks (related to Fig. 4C)

Confocal Z stack images of asters assembled on top of a supported lipid bilayer were obtained using an inverted spinning disc microscope with a 60x objective (1.49 NA): 80 z-sections were acquired at 0.25-μm intervals. 3D reconstruction was performed with *Volume Viewer* ImageJ plugin.

Immunofluorescence of Fixed *Xenopus* Zygotes (see Fig. 1D and fig. S4)

Embryos were fixed and stained as previously described (*6*). Briefly, embryos were fixed in 50mM EGTA, pH 6.8, 10% H_2O, 90% methanol for 24 hrs at room temperature with gentle shaking. Prior to staining, embryos were rehydrated in a series of steps—25%, 50% 75%, 100% TBS (50 mM Tris, pH 7.5, 150 mM NaCl) /Methanol—and then hemisected in TBS on an agarose cushion using a small piece of razor blade. Embryos were bleached overnight in a solution of 1% H_2O_2, 5% formamide, 0.5x SSC (75mM NaCl and 8mM sodium citrate, pH 7). Embryos were incubated with directly labeled antibodies for at least 24 hrs at 4° C with very gentle shaking. Antibodies were diluted into TBSN (10mM Tris-HCl, pH 7.4, 155mM NaCl, 0.1% Igepal CA-630) + 1% BSA + 2% FCS + 0.1% Azide. After antibody incubation, embryos were washed in TBSN for at least 48 hrs (with several buffer changes), then washed 1X in TBS and 2X in methanol for 20 min each. Embryos were cleared in Murray Clear solution (benzyl benzoate, part benzyl alcohol 2:1) and mounted in metal slides (1.2mm thick) with a hole in the center. The hole was closed on the bottom with a Parafilm-attached coverslip.

Directly labeled antibodies were used at approximately the following concentrations: Alexa488-tubulin (1-2µg/mL), Alexa647-AurB kinase (0.5µg/mL), Alexa568-Kif23 (1-2µg/mL), Alexa568-anillin (1-2µg/mL).

Aurora Kinase B Inhibition in *Xenopus* Zygotes (see fig. S4)

Eggs were fertilized, dejellyed with 2% cysteine in MMR (110mM NaCl, 2mM KCl, 1mM $MgCl_2$, 2mM $CaCl_2$, 2mM $NaHCO_3$, 5mM K-Hepes, pH 7.8), and microinjected with ZM447439 (Aurora B kinase inhibitor) before or after metaphase of 1st mitosis (either 50-55 or 75-80 minutes post fertilization). For injections, eggs were placed in Petri dishes, with mesh attached to the bottom, containing 5% Ficoll in 0.1X MMR. Eggs were injected with calibrated needles using an air-pressure microinjector (Narishige). Needles (~1.2mm initial diameter) were pulled with a Micropipette Puller (Sutter Instrument Company) and calibrated to inject 10nL of sample. Briefly, the tips of needles were broken with a pair of forceps under a dissection microscope and the time of the injection pulse was varied until the desired injection volume was reached. ZM447439 (10mM) was dissolved in 10mM glycine (pH 7); control buffer injections were done with 10mM glycine (pH 7). Cytokinesis was completely inhibited after early injections (50-55 min) and no furrows (2/10) or shallow, abortive cleavage was observed after late injections (8/10 embryos). Immunofluorescence of zygotes injected after metaphase (75-80 min) showed disruption in AAIZ formation and CPC recruitment (fig. S4). Control buffer injections had no effect (6/6 embryos), confirming the expected AurkB requirement (*8*).

Supplementary Text

Model for CPC Recruitment and Transport at AAIZs

The simplest model that is consistent with our data is one in which the CPC is targeted to regions of antiparallel overlap by interaction with Kif20AE; once recruited there, it is transported to the center of the overlap region by interaction with Kif4A. In this model Kif4A acts as a transport motor, at least over a limited region. Kif20AE could act as a transport motor, or in some other way. For example it could serve as a recognition element for antiparallel overlapping microtubules that lacks transport activity, and instead promotes targeting of CPC to the overlap by diffusion and trapping. It could also act as an allosteric activator of the CPC without microtubule binding activity. Its somatic homolog Kif20A has been shown to possess microtubule-stimulated ATPase activity, but has not been shown to possess transport motor activity (*26*). Our reasons for proposing the simple model are listed below. We note that our data do not exclude less direct roles for either kinesin, where the kinesin need not directly interact with the CPC. For example, Kif4A could act to somehow modify the microtubule tracks in the overlap zone to promote transport of CPC by some other kinesin, for example Kif20AE. It is difficult, in general, to rule out indirect actions in a complex system. Pure protein reconstitution is required to fully address the function of the two kinesins in CPC targeting.

The following observations from the depletion/addback experiments lead us to propose the two-kinesin mechanism above for CPC transport:

1. Kif20AE depletion leads to complete block of CPC recruitment to antiparallel microtubule overlaps (Fig. 2A).
2. Kif4A depletion does not lead to block of CPC or Kif20AE recruitment (Fig. 2A), but only blocks transport of CPC within antiparallel microtubule overlaps (Fig. 2, E and F).
3. The localizations of Kif20AE and Kif4A are distinct: Kif20AE co-localized with the CPC in the center (Fig. 2C), while Kif4A localized more broadly on antiparallel microtubule overlaps (Fig. 2D). This suggests that the CPC-Kif20AE complex could be a cargo of the Kif4A transport motor.

We hypothesize that a two-kinesin mechanism is required to ensure precise localization of the CPC to the cleavage plane in egg cells where the spatial scale is very large, and antiparallel overlaps are much wider (up to tens of μms) than in small somatic cells (2-3μm). Further experiments are required to better define the spatial extent of antiparallel overlaps, and the factors that determine the extent of Kif4A and CPC localization relative to these overlaps.

Model for Orientation of Actin Cables at the Surface of Bilayer

We believe that our system reconstitutes a pre-cytokinesis state where the CPC-positive overlap zones signal to the cortex to position the cleavage furrow. Thus the orientation of actin cables we observe in our system corresponds with actin organization at early anaphase in live cells, and not the cytokinesis ring itself. This alignment of cortical actin cables perpendicular to the putative cleavage plane is consistent with observations using fluorescently labeled actin filaments in somatic cells (*22*). It has been proposed that actin filaments undergo reorganization at the cleavage site from a parallel alignment along the spindle axis to an orthogonal one as cells proceed from anaphase to cytokinesis. Actin cables traversing the cytoplasm that connected the dorsal part of the cleavage furrow to the ventral side have been reported in dividing mammalian cells (*27*).

Extended Acknowledgements

We thank Ryoma Ohi for the generous gift of Aurora B antibody and David Burgess for the Lifeact-GFP construct and protein; Edwin Tan for initiating Kif20A and Kif23 antibody projects and help with tubulin preparation; David Miyamoto for initiating the Xklp1/Kif4 antibody project; Himanish Basu for contributing towards optimization of the supported lipid bilayer preparation. We thank Jennifer Waters, Lara Petrak, Lauren Piedmont and the Nikon Imaging Center at Harvard Medical School (HMS) for microscopy support; Lynne Chang, Nikon and the Marine Biological Laboratory (MBL) for use of laser scanning confocal and TIRF microscopes; the NXR at MBL for *Xenopus* animals and care. We also thank Calixto Saenz and the Microfluidics Core Facility at HMS for use of their plasma etcher for coverslip cleaning, and Stephen Harrison's lab for providing Sf21 insect cells.

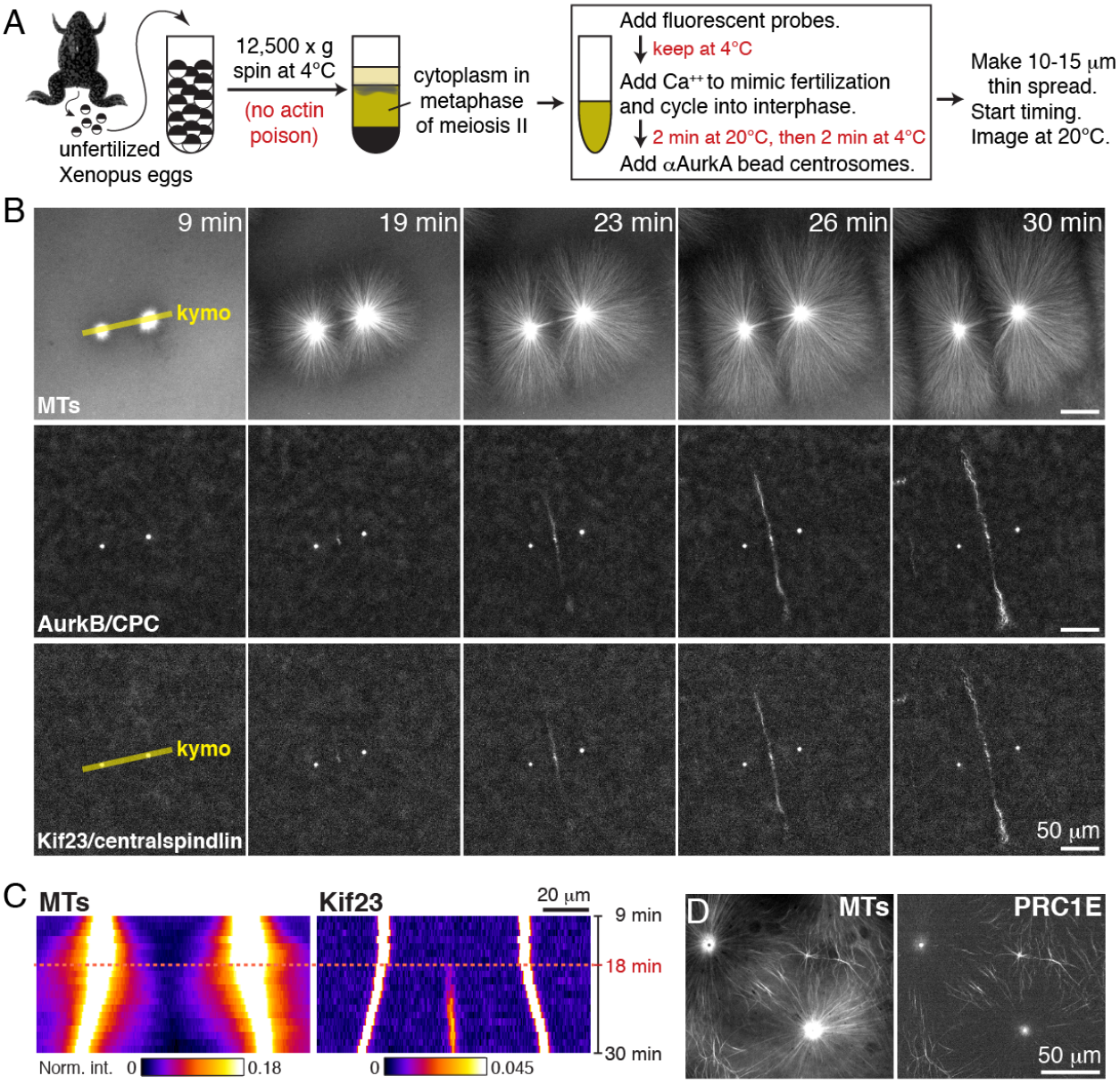

Fig. S1. Aster assembly assay in *Xenopus* egg cytoplasm. (A) Experimental workflow. Undiluted cytoplasm with intact actin was prepared from *Xenopus* eggs (*3*). Extract was supplemented with fluorescent probes and then released from meiotic arrest into interphase by calcium addition, which mimics fertilization. Beads coated with Aurora A kinase (AurkA) antibody that mimic centrosomes (*4*) were added, a thin extract layer was spread between PEG-passivated coverslips and immediately imaged. **(B)** Widefield time-lapse showing recruitment of AurkB (CPC subunit) and Kif23 (Centralspindlin subunit) to an aster-aster interaction zone (AAIZ); image sequence related to Fig. 1, B and C. **(C)** Kymographs along the bead-bead axis (yellow lines in (B)) showing aster growth and interaction (MTs, left) and recruitment of Kif23 where asters interact (right, from 18 min). Similar profiles were obtained for AurkB recruitment. **(D)** Spinning disc confocal image of AAIZs at 30min with the embryonic paralog of PRC1 localized (GFP-PRC1E).

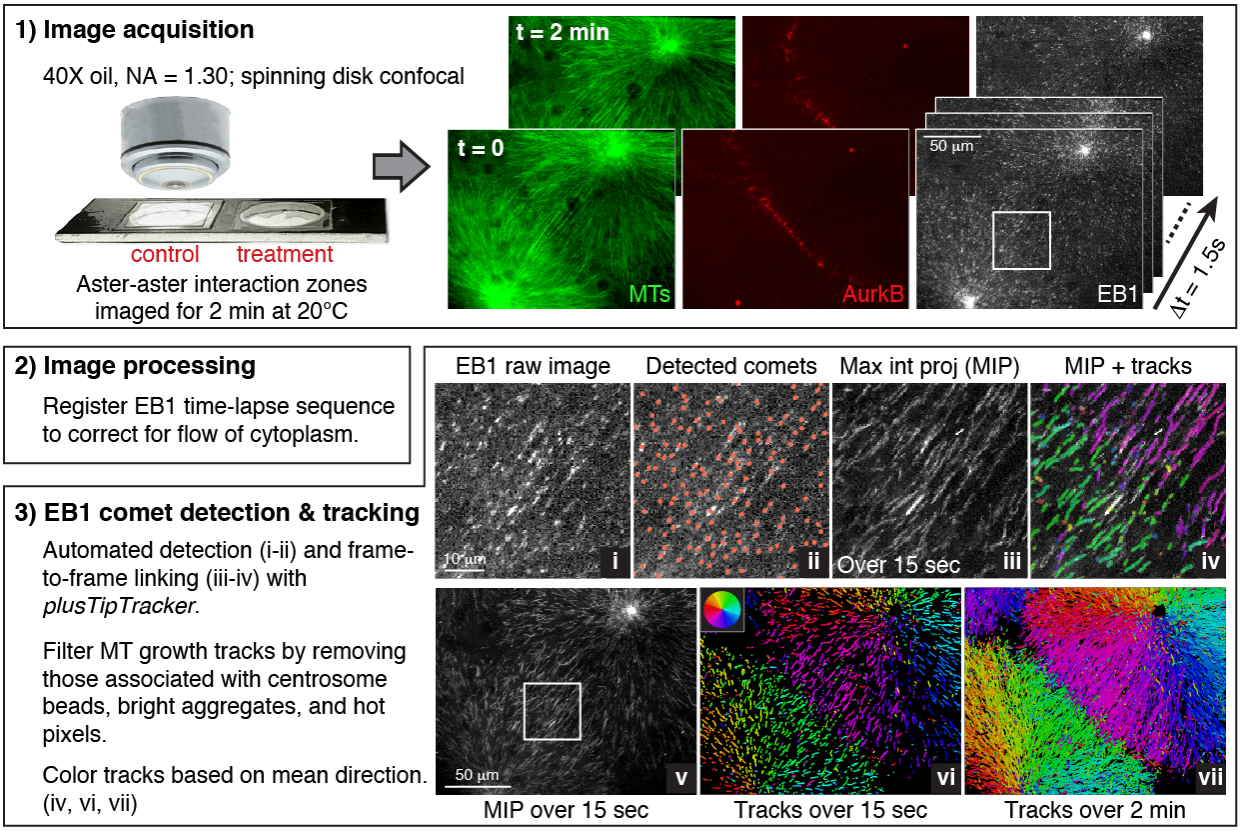

Fig. S2. Microtubule plus tip tracking using EB1-GFP protein. (1) Asters were assembled between PEG-passivated coverslips, simultaneously for control and treatment samples (e.g. AurkB inhibition). Multiple AAIZs were imaged between 20 and 50 min of the assembly reaction, alternating between control and treatment conditions, using a spinning disc confocal microscope with a 40x oil objective. Time-lapse sequences were acquired of EB1-GFP with 1.5 sec intervals for a total duration of 2 min. Images of tubulin and AurkB were acquired at the beginning and end of each sequence. **(2)** Flow of cytoplasm was corrected by registering EB1 image sequences using the *StackReg* ImageJ plugin. **(3)** The *plusTipTracker* Matlab software was used to perform automated detection and frame-to-frame linking of EB1 to obtain growth tracks (see table S2 for parameters) (*25*). False tracks associated with bright centrosome beads, protein aggregates, and hot pixels in the camera were removed. Tracks were plotted and colored according to their mean direction. Top row images are zoomed up views of area marked by white square in EB1 image in **Step 1**. See Supplementary Methods section "Microtubule Plus Tip Tracking: Image Acquisition, Processing and Analysis" for more detailed description.

(analysis continued from MT plus tip tracking, fig. S2)

4) Interpenetration analysis for a single aster-aster interaction zone (AAIZ)

a. Divide comets (summed over 2 min) into two populations based on direction.
b. Divide space into binned rectangular ROIs perpendicular to interaction zone.
c. Determine population fractions. (Example data for ROI6)

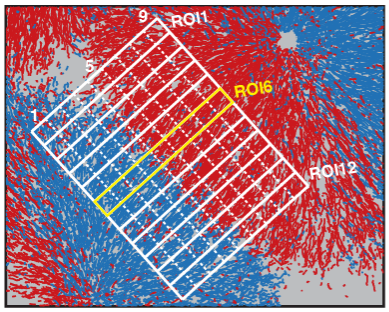

Bin No.	Number of EB1 comets			
	Total	Blue	Red	% Blue
1	265	240	25	90.6
2	279	250	29	89.6
3	308	278	30	90.3
4	351	281	70	80.1
5	282	41	241	14.5
6	268	10	258	3.7
7	255	30	225	11.8
8	265	22	243	8.3
9	301	6	295	2.0

d. Plot population fractions over distance for all ROIs.
e. Remove outlier ROIs (1 & 2).

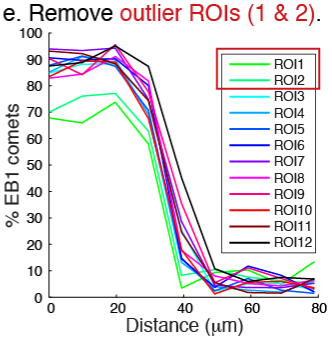

5) Interpenetration analysis for multiple AAIZs

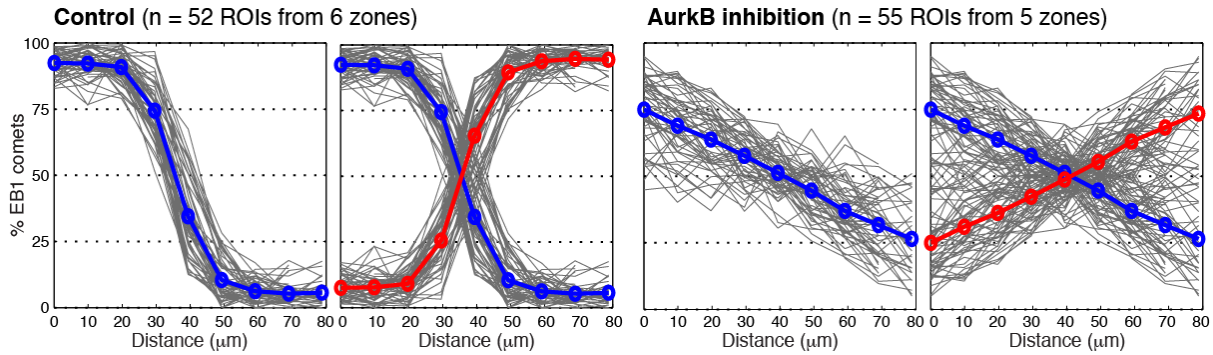

Gray lines -- population fraction data associated with each ROI.
Blue line -- mean fraction of "blue" comets.
Red line -- mean fraction of "red" comets, corresponding to (1 - Blue Fraction).

Same data are displayed in Figure 1F with standard deviation represented by shaded area.

Fig. S3. Aster-aster interpenetration analysis based on tracked microtubule plus ends. See Supplementary Methods section "Aster-Aster Interpenetration Analysis" for description.

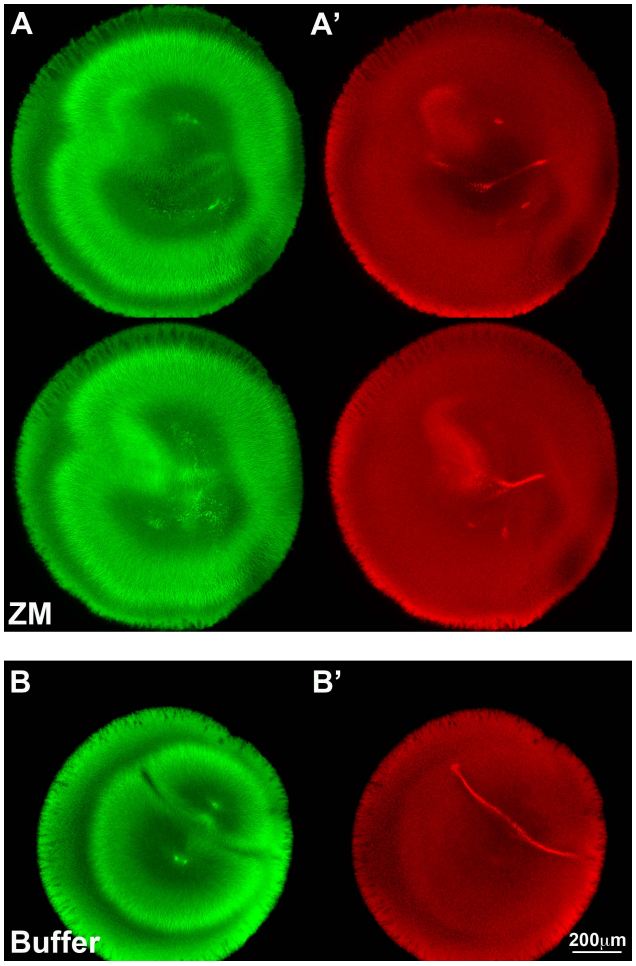

Fig. S4. Aurora B kinase activity is required for organization of the aster-aster interaction zone (AAIZ) in *Xenopus* zygotes. Fertilized *Xenopus* eggs were injected with the Aurora kinase B specific inhibitor ZM447439 (10mM in buffer) or buffer alone after first mitosis and before first cytokinesis (75-80 minutes post fertilization), then fixed, stained for microtubules (green) and AurkB (red), and imaged by confocal microscopy. Similar images were obtained in three biological repeats. **(A, A')** Zygote injected with ZM447439 at 78 min and fixed at 130 min. Two focal planes are shown. Note disruption of antiparallel microtubule organization and CPC recruitment between the growing asters. Aster growth was not affected. **(B, B')** Zygote injected with control buffer at 73 min and fixed at 110 min. Antiparallel microtubule organization and CPC recruitment were not affected. Note buffer injection could move or distort the asters, however organization of the AAIZ with AurkB in zone was maintained.

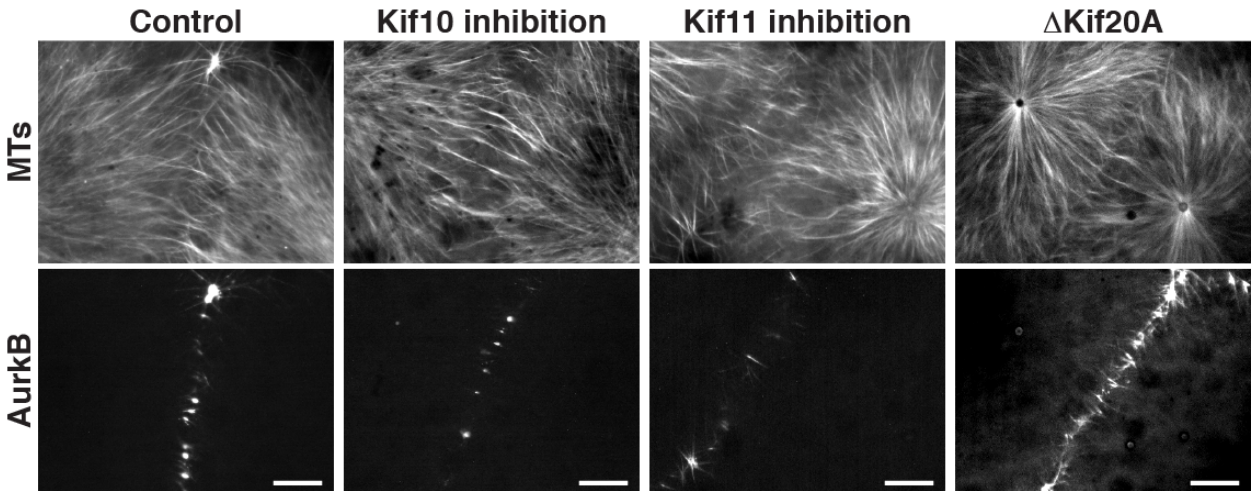

Fig. S5. Small molecule inhibition and immunodepletion of kinesin candidates that had no effect on AAIZ formation and CPC localization. Asters were assembled between PEG-passivated coverslips, and AAIZs were imaged after 30 min. Representative spinning disc confocal images of MTs and AurkB at AAIZs after treatment with DMSO control, 100μM GSK-923295 (a Kif10/CenpE inhibitor; experiments with mitotic spindles in egg extracts and *Xenopus* tissue culture cells confirmed expected activity of this compound, i.e. displacement of mitotic chromosomes from the metaphase plate (*28*)), 100μM STLC (S-trityl-l-cysteine, a Kif11/Eg5 inhibitor (*29*)), or depletion of the somatic Kif20A motor, as labeled above. Representative control depletion with random IgG is shown in Fig. 2A. Bar, 20 μm.

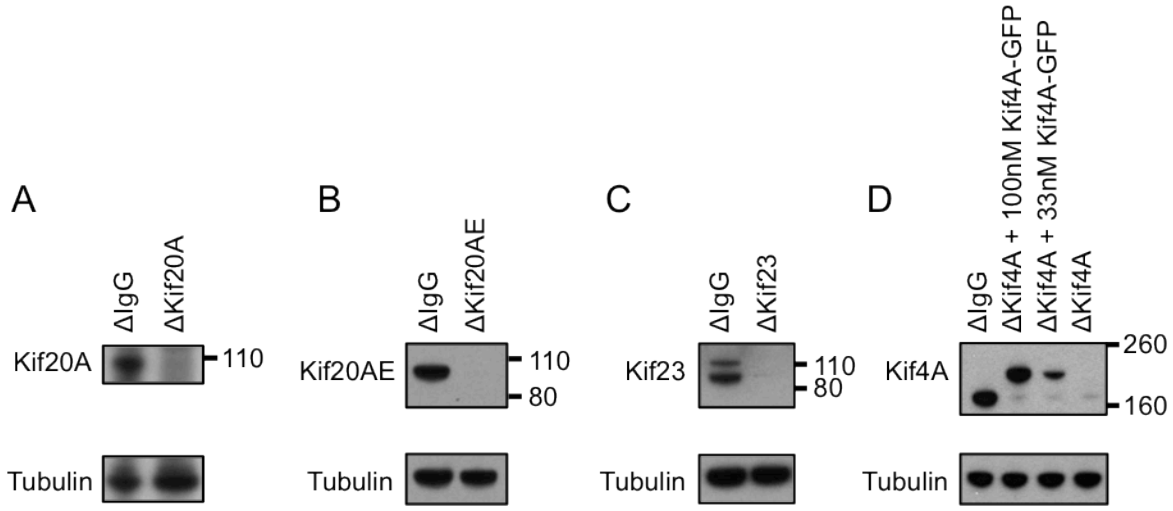

Fig. S6. Immunoblots showing immunodepletion of *Xenopus laevis* kinesin candidates.
(A) Kif20A (Mklp2 or Rabkinesin-6, ~101 kD). **(B)** Kif20AE (~88 kD), an embryonic paralog of Kif20A in *Xenopus*. **(C)** Kif23 (Mklp1, a subunit of Centralspindlin complex, ~90 kD).
(D) Kif4A (~139 kD) depletion was rescued by adding back 100nM recombinant Kif4A-GFP (~168 kD).

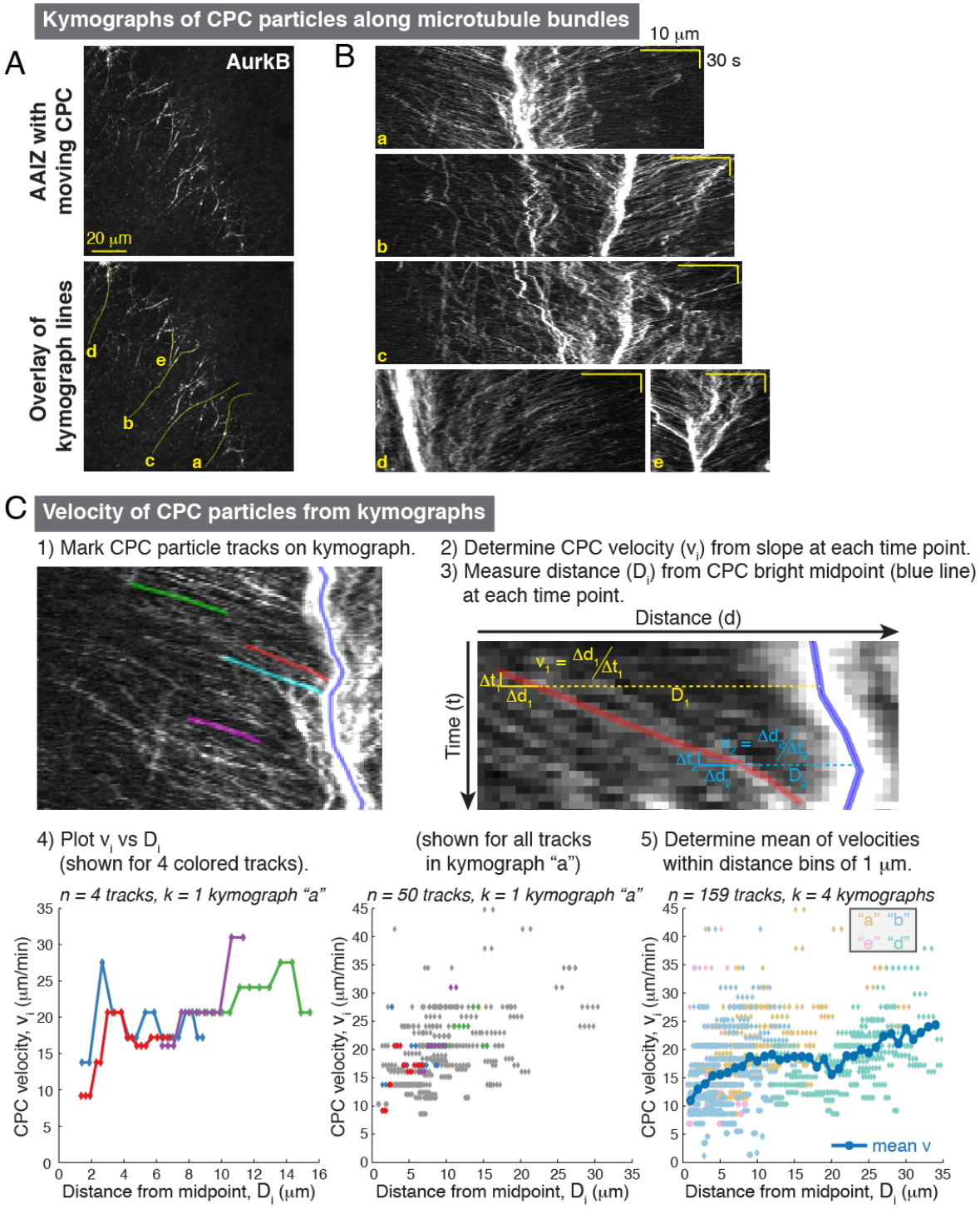

Fig. S7. Measuring velocity of directed CPC movement on the antiparallel microtubule overlaps at the aster-aster interaction zones (AAIZs). (A) Spinning disc confocal image of CPC visualized with Alexa647-labeled antibody against AurkB at an AAIZ at the beginning of a time-lapse sequence *(top)*. Segmented lines for kymographs are overlaid in yellow *(bottom)*. **(B)** Kymographs generated from the time-lapse (total duration of 170 sec with 1.43 sec intervals) corresponding to lines (a-e) in (A). **(C)** Procedure for obtaining CPC velocity as a function of distance from the CPC bright midpoint. See Supplementary Methods section "Velocity Measurements for CPC Movement" for more detailed description.

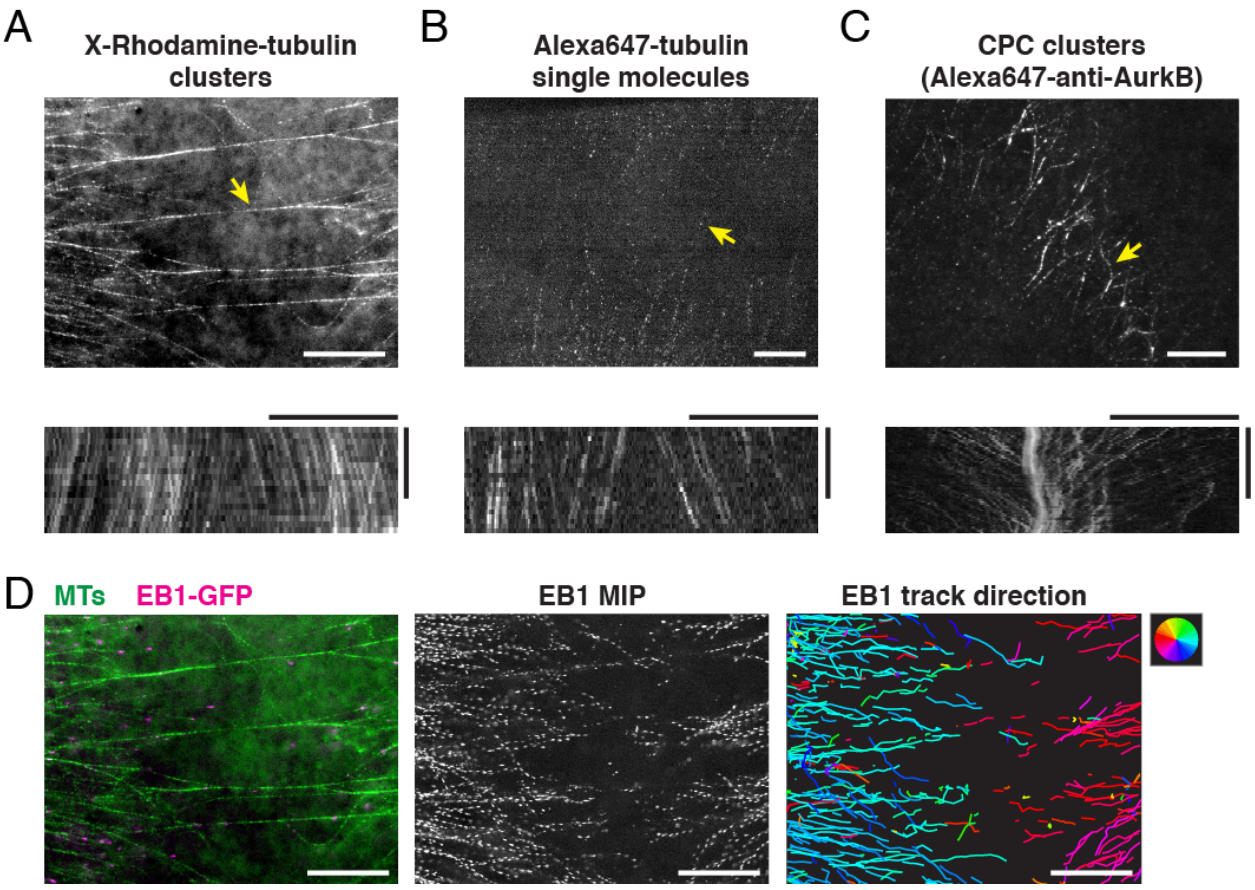

Fig. S8. Tubulin speckle imaging shows antiparallel microtubules sliding outward from overlap center. (A) Tubulin speckles were formed by uneven incorporation of the relatively hydrophobic X-rhodamine-tubulin into microtubules. The movement of these X-rhodamine tubulin clusters was imaged with time-lapse widefield microscopy at 5 sec intervals (movie S6). **(B)** Tubulin speckles were formed by single-molecule level incorporation of Alexa647-tubulin into microtubules. Time-lapse spinning disc confocal images were taken at 4 sec intervals (movie S8). **(C)** CPC clusters were visualized using Alexa647-IgG against AurkB and imaged with time-lapse spinning disc confocal microscopy at 1.3 sec intervals (same data as shown in fig. S7A, movie S4). **(A-C)** Still images from each time-lapse sequence *(top)*. Kymographs along the MT overlap bundles indicated by yellow arrow *(bottom)*. Horizontal bars, 20 μm. Vertical bars, 1 min. Kymographs show that while microtubules slide slowly outwards from the overlap centers at <5 μm/min, CPC clusters move inwards at 10-25 μm/min towards overlap center. This confirms that the fast inwards movement of the CPC is indeed motor-driven transport along microtubules. **(D)** Overlay of EB1-GFP image (magenta) on tubulin image (green) shown in (A); a still image from movie S7 *(left)*. Maximum intensity projection of EB1 images *(middle),* and EB1 tracks colored by their mean direction *(right)* over the first half (2.5 min) of movie S7. Movie 7 illustrates the relationship between microtubule plus end growth (i.e. EB1 comet movement) and formation of antiparallel bundles. Horizontal bars, 20 μm.

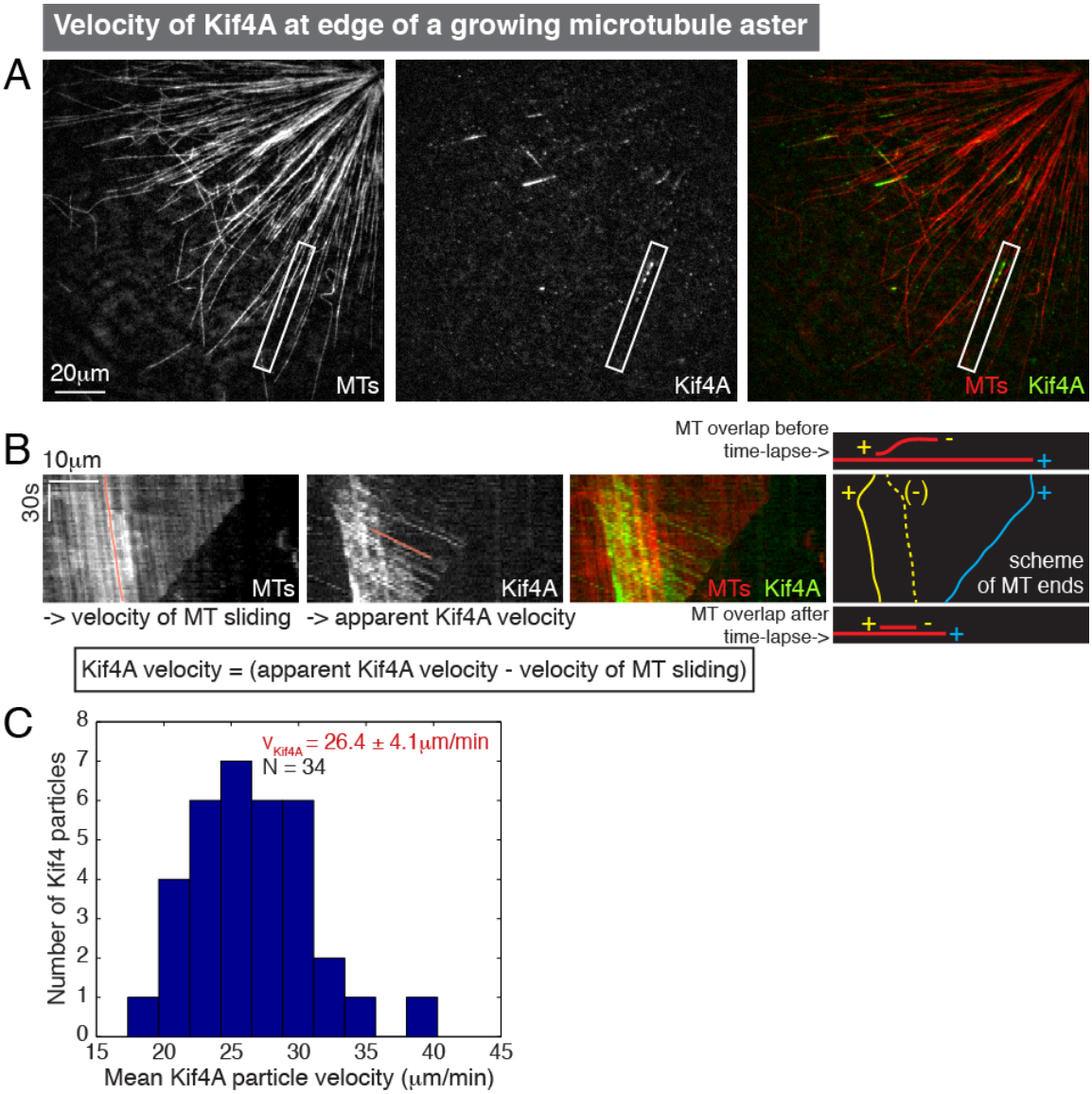

Fig. S9. Measuring the plus-end directed velocity of the kinesin Kif4A. (A) Expanding aster partially adhered to κ-casein coated coverslip with microtubules (Alexa647-tubulin; red) and Kif4A-GFP (green) visualized. TIRF image from a time-lapse sequence acquired using 2.1sec intervals for a total duration of 7.3min. **(B)** Kymographs of a microtubules (red) and Kif4A (green) along a microtubule that had a free plus end but was also part of an anti-parallel overlap (box in A). Scheme *(right)* shows the geometry of microtubules (red lines) before and after the time-lapse (top and bottom panels, respectively), and the inferred plus ends of the anti-parallel microtubules (yellow and blue solid lines); an antiparallel overlap is formed between the solid and dashed yellow lines. Apparent Kif4A velocity (measured from Kif4A kymographs) was corrected by velocity of microtubule sliding (measured from microtubule kymographs). **(C)** The velocity distribution of Kif4A moving on microtubules that are not part of AAIZs. Kif4A has a mean velocity of 26.4 ± 4.1 μm/min (mean±SD, N = 34 tracked Kif4A particles), an estimate for maximum velocity in our extract system.

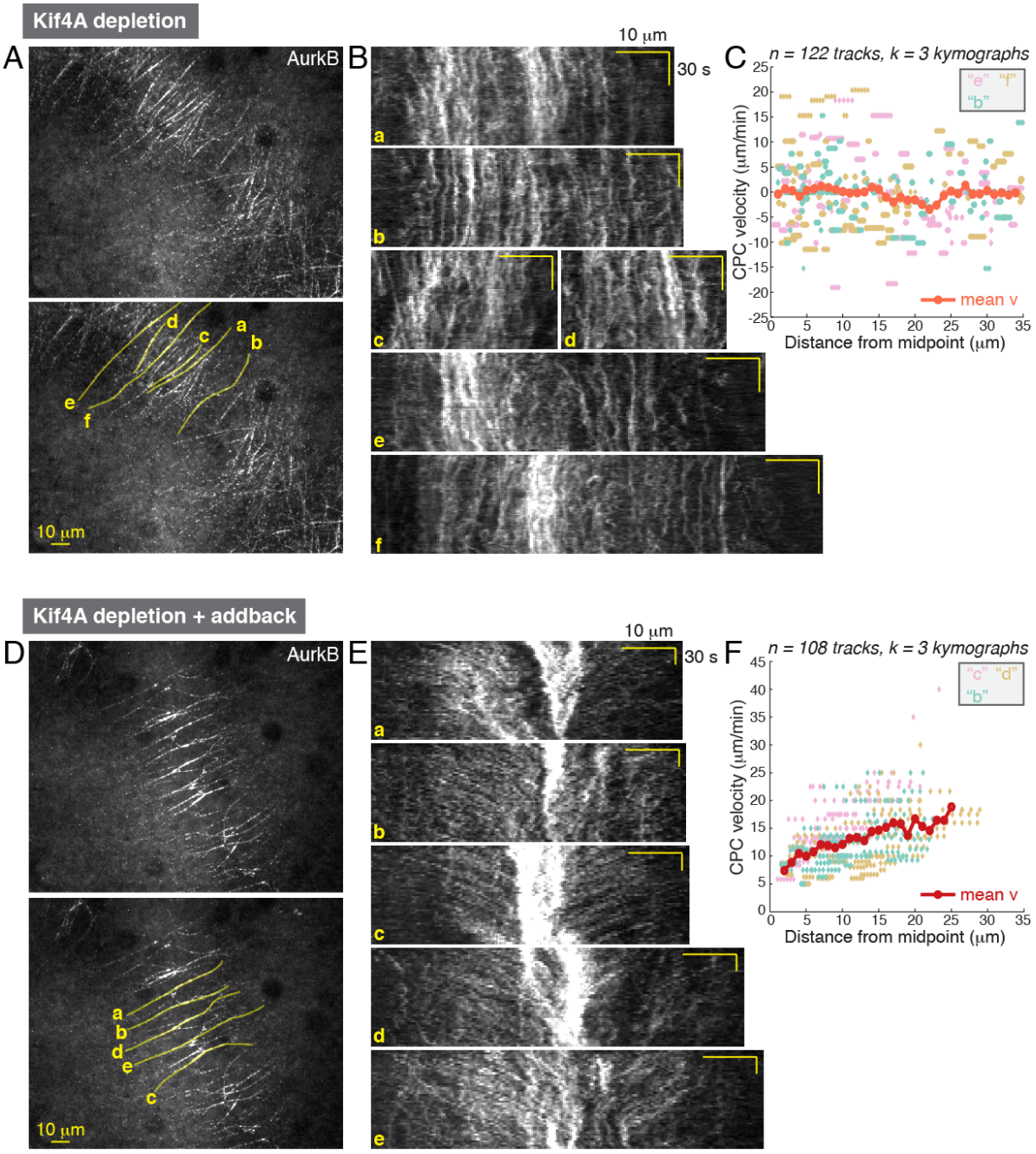

Fig. S10. Directed CPC movement on antiparallel microtubule bundles requires the kinesin Kif4A. Same analysis of CPC movement as described in fig. S7 was performed on extracts where Kif4A was depleted (A to C) and where Kif4A depletion was followed by addback of purified Kif4A-GFP (D to F). **(A,D)** Spinning disc confocal image of CPC visualized with Alexa647-labeled antibody against AurkB at an AAIZ at the beginning of a time-lapse sequence *(top)*. Segmented lines for kymographs are overlaid in yellow *(bottom)*. **(B,E)** Kymographs generated from the time-lapse: total duration of 90 sec with 1.29 sec intervals for (B) and total duration of 177 sec with 3.94 sec intervals for (E). **(C,F)** Instantaneous CPC velocities (v_i) plotted against distance from bright CPC midpoint (D_i) determined from 3 kymographs, with the mean velocity calculated for each 1 μm distance bin.

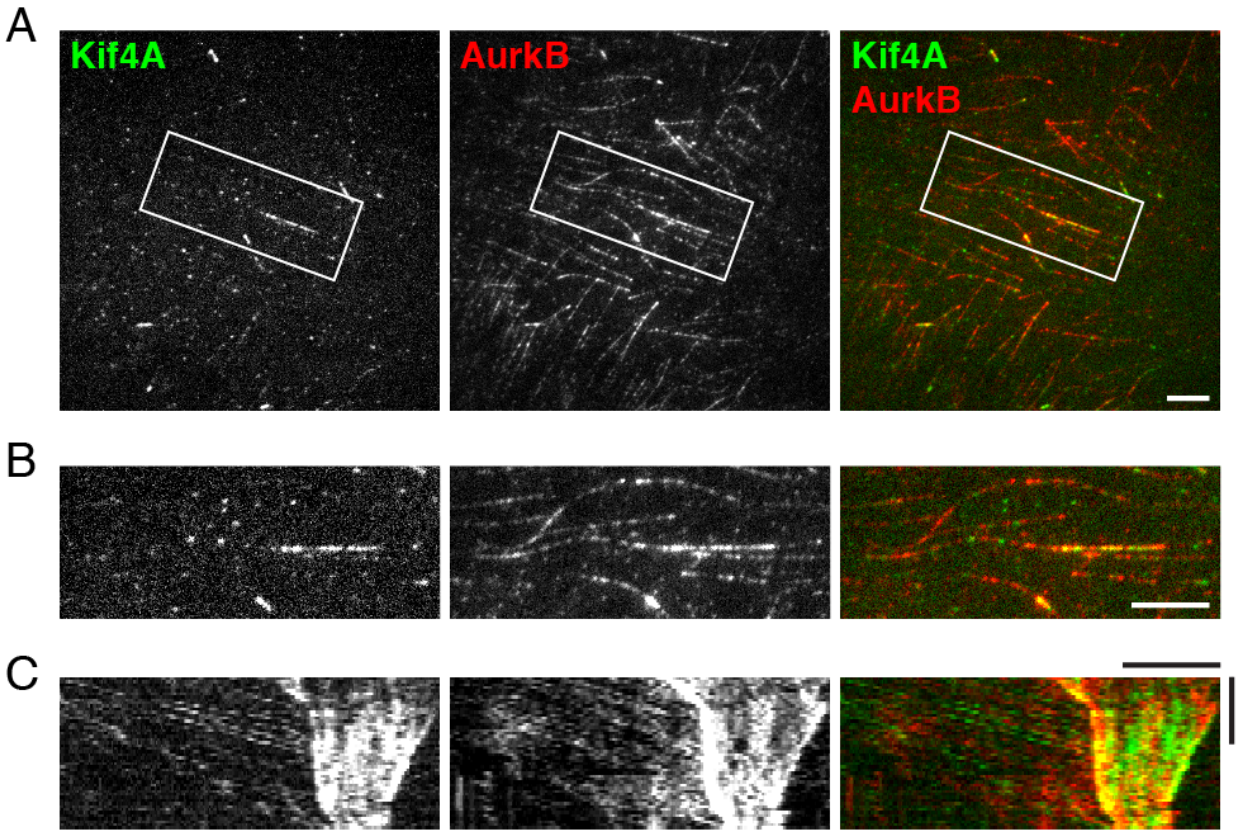

Fig. S11. Partial co-localization of moving Kif4A and moving CPC clusters at AAIZ. **(A)** Stills from a time-lapse, two-color TIRF image sequence taken with a 2.73 sec time interval, and a time delay of ~1.36 sec between acquisition in the two channels. Kif4A-GFP was added at 3nM on top of endogenous Kif4A present in extract (left, green). Alexa647-anti-AurkB was added at 0.1μg/mL to probe for endogenous CPC (middle, red). The right shows a merged image. **(B)** 2x zoom-up of rectangle in (A) highlighting an antiparallel microtubule overlap and partial co-localization of the two probes. **(C)** Kymographs along the antiparallel MT overlap shown in (B). Note that the two probes move inwards at very similar rates (visualized as parallel lines in the kymographs). The fast-moving clusters localized at the outside of the AAIZ were moving inwards at ~25 μm/min in this example. We noted more co-localization between Kif4A-GFP and CPC clusters in static and slow moving clusters near the center. In fast moving clusters, the lines of Kif4A and CPC were staggered, presumably due to the time delay between acquisition in the green and red channels. Horizontal bars, 10 μm. Vertical bars, 1 min.

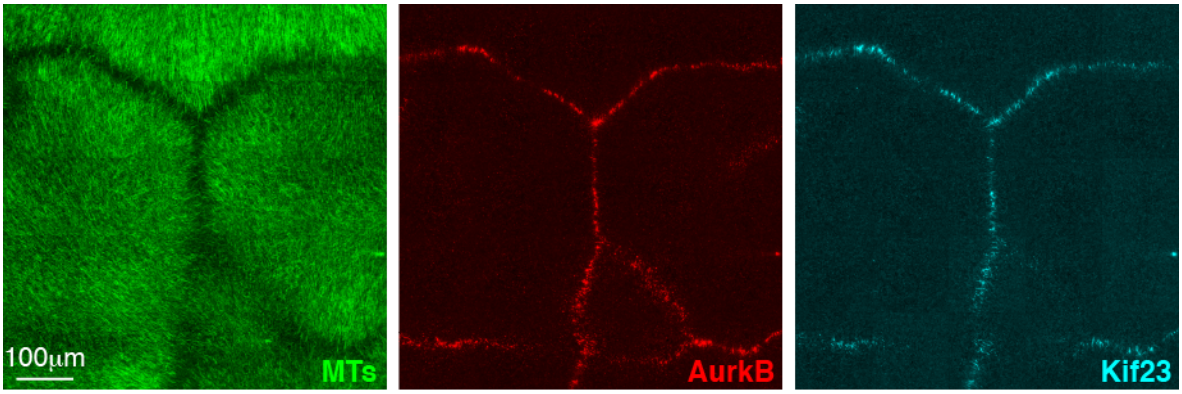

Fig. S12. The CPC and Centralspindlin complexes co-localize at AAIZs on model plasma membranes. Experimental setup as per Fig. 3A. TIRF images from 5x5 adjacent fields were corrected for uneven illumination and stitched (*5*). Microtubules (green), CPC (AurkB, red), Centralspindlin (Kif23, cyan).

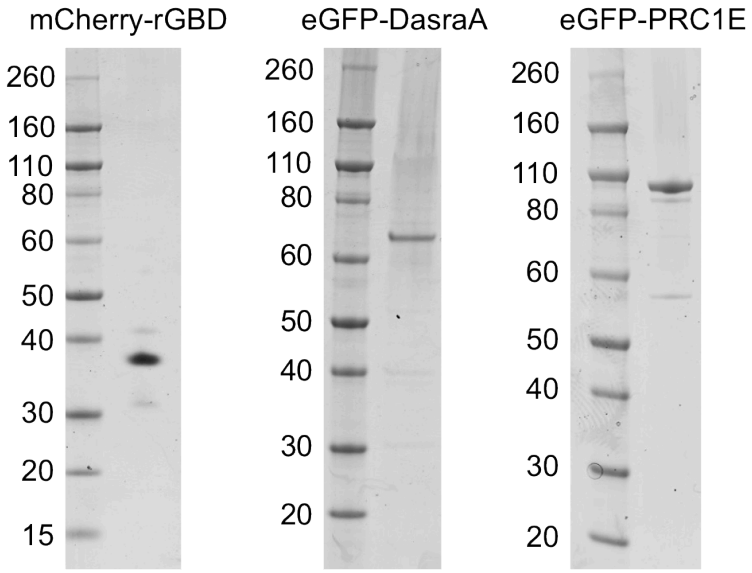

Fig. S13. Coomassie-stained SDS gels of purified proteins with cloning and purification methods established in this study. Theoretical molecular weights of the protein constructs are: 39 kD (mCherry-rGBD), 61 kD (eGFP-DasraA), and 96 kD (eGFP-PRC1E).

Table S1.
List of *Xenopus laevis* protein sequences studied in this paper.

Name	Description/Alternate names	NCBI GI number
AurkA	Aurora kinase A	148236543
AurkB	Aurora kinase B	147899288
DasraA	Borealin-2	148232132
PRC1E	Embryonic paralog of PRC1 (42% identity by sequence)	148231955
Kif4A	Chromokinesin, Xklp1	18202613
Kif20A	Mklp2, Rabkinesin-6	147902220
Kif20AE	Embryonic paralog of Kif20A (41% identity by sequence)	169642006 (starting at "MDSRN")
Kif23	Mklp1, CHO1	148222381

Table S2.
Parameters for automated detection and tracking of EB1 comets using *plusTipTracker* (*25*).

Image sequence calibrations	
Pixel size	0.3284 µm
Frame rate	1.5 s

Detection parameters	
Method	Watershed-based
Sigma 1	1
Sigma 2	7
K	1-2.5

Tracking parameters	
Maximum gap length	2 frames
Minimum sub-track length	3 frames
Minimum search radius	1 pixel
Maximum search radius	3 pixels
Maximum forward angle	30°
Minimum forward angle	10°
Fluctuation radius	1 pixel
Maximum shrinkage factor	1

Movie S1. Aster outgrowth and interaction in *Xenopus* egg cytoplasm (related to Fig. 1B and fig. S1B). Asters were nucleated from beads coated with Aurora A kinase antibody on PEG-passivated coverslips. Where neighboring asters met, an aster-aster interaction zone (AAIZ) formed that recruited the chromosomal passenger complex (CPC). Widefield time-lapse sequence was acquired starting at 9 min of aster assembly reaction using a 20X objective, with 1 min intervals. Microtubules (green), CPC (Aurora B kinase subunit, red). Field of view: 277µm x 277µm. Duration: 21 min (420x speed).

Movie S2. Block to microtubule interpenetration at an AAIZ (related to Fig. 2E, top panel, and fig. S2). Growth of microtubule plus ends was visualized with EB1-GFP at an AAIZ on PEG-passivated coverslips. Aster #1 at top right corner, aster #2 at bottom left corner, aster #3 at top left corner. Confocal time-lapse sequence was acquired starting at 20 minutes of aster assembly reaction using a 40X oil objective, with 1.5 sec intervals. Field of view: 198µm x 157µm. Duration: 2 min (24x speed).

Movie S3. Block to microtubule interpenetration requires Aurora B kinase (related to Fig. 2E, bottom panel). Growth of microtubule plus ends was visualized with EB1-GFP at an AAIZ in the presence of Aurora B kinase inhibitor (ZM447439) on PEG-passivated coverslips. Aster #1 on the left, aster #2 on the right. Confocal time-lapse sequence was acquired starting at 20 minutes of aster assembly reaction using a 40X oil objective, with 1.5 sec intervals. Field of view: 193µm x 157µm. Duration: 2 min (24x speed).

Movie S4. Directed CPC movement on antiparallel microtubule bundles at an AAIZ (related to Fig. 2E and fig. S7). CPC recruitment and movement at the AAIZ was visualized using Aurora B kinase antibody on PEG-passivated coverslips. Aster #1 at top right corner, aster #2 at bottom left corner. Confocal time-lapse sequence was acquired starting at 50 minutes of aster assembly reaction using a 40X oil objective, with 1.44 sec intervals. Field of view: 122µm x 122µm. Duration: 1.5 min (24x speed).

Movie S5. Directed CPC motility at an AAIZ requires Kif4A (related to Fig. 2E and fig. S10, A to C). CPC recruitment and movement at the AAIZ in Kif4A depleted cytoplasm was visualized using Aurora B kinase antibody on PEG-passivated coverslips. Aster #1 at top right corner, aster #2 at bottom left corner. Confocal time-lapse sequence was acquired starting at 50 minutes of aster assembly reaction using a 40X oil objective, with 1.31 sec intervals. Field of view: 122µm x 122µm. Duration: 1.5 min (24x speed).

Movie S6. Antiparallel sliding of microtubules at AAIZ (widefield) (related to fig. S8A). Microtubule sliding was visualized using clusters of unevenly incorporated X-rhodamine-tubulin on PEG-passivated coverslips. Aster #1 on the left, aster #2 on the right. Widefield time-lapse sequence was acquired starting at 50 minutes of aster assembly reaction using a 100X oil objective, with 5 sec intervals. Note slow outwards sliding of microtubules away from center of antiparallel overlap. Field of view: 87.0µm x 66.3µm. Duration: 5 min (40x speed).

Movie S7. Antiparallel sliding and plus end growth of microtubules at AAIZ (widefield) (related to fig. S8D). Same image sequence as shown in movie S6, but with the EB1 channel added to visualize growing microtubule plus ends. Note the transition from parallel bundles in each aster to antiparallel bundles in the AAIZ. Some EB1 comets entered the antiparallel bundles where they disappeared after tracking along them for a few frames; other EB1 comets disappeared outside of a bundle. X-rhodamine-tubulin (green), EB1-GFP (magenta). Field of view: 87.0µm x 66.3µm. Duration: 5 min (40x speed).

Movie S8. Antiparallel sliding of microtubules at AAIZ (confocal) (related to fig. S8B). Microtubule sliding was visualized using speckle-level of Alexa647-tubulin on PEG-passivated coverslips. Aster #1 at the top, aster #2 at the bottom. Confocal time-lapse sequence was acquired starting at 50 minutes of aster assembly reaction using a 60X oil objective, with 4 sec intervals. Field of view: 138µm x 105µm. Duration: 5.5 min (60x speed).

Movie S9. Organization of F-actin at an AAIZ on a model membrane (related to Fig. 4D, bottom middle panel). F-actin was visualized using Lifeact-GFP on lipid bilayer-coated coverslip. TIRF time-lapse sequence was acquired starting at 50 minutes of aster assembly reaction using a 60X TIRF objective, with 3 sec intervals. Field of view: 136µm x 136µm. Duration: 4 min (120x speed).

Movie S10. Organization of anillin at an AAIZ on a model membrane (related to Fig. 4E, middle panel). Anillin was visualized using directly labeled antibody on lipid bilayer-coated coverslip. TIRF time-lapse sequence was acquired starting at 50 minutes of aster assembly reaction using a 60X TIRF objective, with 3 sec intervals. Field of view: 136µm x 136µm. Duration: 4 min (120x speed).